

## Coexistence curve, compressibility, and the equation of state of xenon near the critical point\*

W. T. Estler,<sup>†</sup> R. Hocken,<sup>‡</sup> T. Charlton, and L. R. Wilcox

Physics Department, S.U.N.Y. at Stony Brook, Stony Brook, New York 11790

(Received 26 February 1975)

Optical interferometric measurements which determine the equation of state of xenon in the neighborhood of the critical point are described. Analysis of Fraunhofer interference patterns from a thin slab of fluid yields data pairs: optical phase  $\psi_+ = \rho - \kappa_T \mu$  and isothermal compressibility  $\kappa_T$ , along isotherms in the temperature range  $-10^{-4} < \epsilon < 10^{-4}$ , where  $\epsilon = (T - T_c)/T_c$ . Experimental data are analyzed in terms of a new parametric transformation of thermodynamic variables, based on the static scaling hypothesis of Widom, which requires that  $d \ln \psi_+ / d \ln \kappa_T = -(\beta/\gamma)W(\theta)$ , where  $\theta = \epsilon \kappa_T^{1/\gamma}$ . On the critical isotherm,  $\epsilon = 0$ , we expect that  $\ln \psi_+ = \text{const} - (\beta/\gamma) \ln \kappa_T$ . This accords with observation and yields a sharp determination of  $T_c$  which is decoupled from other parameters. The data are well represented by the bilinear form  $W(\theta) = (1 - \theta/\theta_x)/(1 - \theta/\theta_0)$  where  $\theta = \theta_0$  on the critical isochore and  $\theta_x$  on the coexistence boundary. This is integrated to yield the parametric equation of state  $\psi_+ = Y_0^\beta R^\beta (1 - \theta/\theta_0)^{\beta\Delta}$ , where  $R = \kappa_T^{-1/\gamma}$ . A six-parameter fit to 1200 data points yields  $T_c = T_c(\text{lab}) \pm 0.0001^\circ\text{C}$ ,  $\beta = 0.3583 \pm 0.0002$ ,  $\gamma = 1.2296 \pm 0.0005$ ,  $\theta_0 = 0.1101 \pm 0.0003$ ,  $Y_0^\beta = 0.4203 \pm 0.0004$ , and  $\Delta = 3.869 \pm 0.001$ . This implies  $\beta\Delta = 1.386 \pm 0.001$ , which differs significantly from the value  $\beta\Delta = \frac{3}{2}$  implied by a five-parameter transformation suggested by Ho and Litster. The coexistence curve is measured in the range  $10^{-5} < |\epsilon| < 5 \times 10^{-2}$ , and fitted by the power law  $(\rho_L - \rho_G)/\rho_c = B(-\epsilon)^\beta$ , with the result  $\beta = 0.344 \pm 0.003$  and  $B = 3.51 \pm 0.05$ . Systematic deviations indicate that  $\beta$  increases for large  $|\epsilon|$ . A fit with the form  $(\rho_L - \rho_G)/\rho_c = B(-\epsilon)^\beta + A(-\epsilon)^{\beta'}$  yields significant improvement, with  $\beta = 0.332 \pm 0.001$ ,  $B = 3.042 \pm 0.03$ ,  $\beta' = 0.61 \pm 0.02$ , and  $A = 0.93 \pm 0.04$ . The disagreement between this  $\beta$  and the  $\beta$  obtained from fitting the Fraunhofer data will be discussed in the text. The coefficient of isothermal compressibility on the critical isochore  $P_c \kappa_T$  is measured in the range  $2.7 \times 10^{-5} < \epsilon < 4 \times 10^{-2}$ , and fitted by the equation  $\kappa_T = P_c \kappa_T = \Gamma \epsilon^{-\gamma}$ . Over the measured range, the data indicate  $\gamma = 1.260 \pm 0.002$  and  $\Gamma = 0.056 \pm 0.001$ . There is evidence that  $\gamma$  depends on the range of fit, and we find  $\gamma = 1.232 \pm 0.006$  for  $\epsilon < 10^{-3}$ , which agrees well with the  $\gamma$  determined from the near-critical Fraunhofer data.

### I. INTRODUCTION

The behavior of a simple fluid in the neighborhood of a liquid-gas phase transition has been the subject of considerable theoretical and experimental interest, due primarily to the remarkable similarity of a condensing fluid to such diverse systems as ferromagnets, ferroelectrics, and binary fluid mixtures.<sup>1</sup> While a complete description of fluid thermodynamic properties requires knowledge of the Helmholtz free energy  $A(\rho, T)$  as a function of its variables, recent studies have come to focus upon the fluid equation of state, of the form  $f(\mu, \rho, T) = 0$ , where the chemical potential is given by  $\mu = (\partial A / \partial \rho)_T$ . An obvious requirement upon the function  $f$  is the description of the various anomalies which serve to define the critical point, and which have come to be described by asymptotic power laws. Of direct interest in the present work are the following:

Coexistence curve:  $(\rho_L - \rho_G)/\rho_c = B(-\epsilon)^\beta$

Critical isotherm:

$$P - P_c \sim \mu - \mu_c = D |\rho - \rho_c|^\delta \text{sgn}(\rho - \rho_c)$$

Isothermal compressibility on the

$$\text{critical isochore: } \kappa_T = P_c \kappa_T = \Gamma \epsilon^{-\gamma},$$

where  $\epsilon = (T - T_c)/T_c$ . (The subscript  $c$  indicates the critical value.)

There has been little progress toward derivation of an adequate equation of state from first principles. With the introduction of the static scaling hypothesis,<sup>2-4</sup> however, considerable progress has been made at the level of phenomenological description. One of us<sup>5</sup> has recently introduced a new scaled representation of the fluid equation of state, based upon the general parametric transformation of state variables introduced by Schofield<sup>6</sup> and Josephson.<sup>7</sup> The new formulation expresses thermodynamic variables in terms of the isothermal compressibility, a stationary optical phase, and the temperature. These quantities are directly measured using an interferometric tech-

nique developed by Wilcox and Balzarini.<sup>8,9</sup>

In Sec. II, we review the new parametric representation, with particular emphasis on a function  $W(\epsilon\kappa_T^{1/\gamma})$  which, if known, determines the equation of state up to an integration constant. In Sec. III we describe the interferometric experiment, and show the connection between experimentally determined quantities and the variables employed in the scaling formulation. In Sec. IV we present results of optical experiments in xenon, analyzed in terms of the parametric representation of Sec. II. In particular, a new operational definition of the critical temperature, suggested by the phenomenology, is applied to optical data and shown to yield a very precise determination of  $T_c$  on a laboratory scale. Knowledge of  $T_c$  and the exponent  $\gamma$  allows a direct test of the static scaling hypothesis, which appears to hold remarkably well for xenon. The scaled equation of state resulting from a simple choice for  $W(\epsilon\kappa_T^{1/\gamma})$  is shown to well represent experimental data. In Sec. V are discussed experimental details, and a discussion of experimental results is presented in Sec. VI.

## II. THE PARAMETRIC REPRESENTATION

Following customary convention in studies of critical phenomena, we introduce the reduced, dimensionless variables

$$\rho^* = \frac{\rho - \rho_c}{\rho_c}, \quad \mu^* = \frac{\rho_c}{P_c} [\mu - M(T)],$$

where  $M(T)$  is the chemical potential on the critical isochore for  $T > T_c$ , and along the coexistence boundary for  $T < T_c$ . For notational simplicity, we henceforth drop (\*) from reduced quantities, unless otherwise noted.

We choose to write the parametric transformation of thermodynamic variables in the form<sup>5</sup>

$$\mu = R^\gamma (\beta/\gamma) Y^\beta W(\theta), \quad (1)$$

$$\rho = Y^\beta [1 + (\beta/\gamma) W(\theta)], \quad (2)$$

$$\epsilon = R\theta, \quad (3)$$

where

$$R = \left( \frac{\partial \mu}{\partial \rho} \right)_\epsilon^{1/\gamma} = \kappa_T^{-1/\gamma}. \quad (4)$$

In these expressions,  $Y = Y(R, \epsilon)$  is a homogeneous function of degree 1, while  $W$  is homogeneous of degree 0, i.e., a function of  $\theta = \epsilon/R$  only. Evidently,

$$Y^\beta = \rho - \kappa_T \mu \quad (5)$$

and

$$\frac{W}{W + \delta - 1} = \frac{\mu/\rho}{(\partial \mu / \partial \rho)_\epsilon}, \quad (6)$$

where we have made use of the scaling relation  $\delta - 1 = \gamma/\beta$ . As will be shown in Sec. III, the function  $Y^\beta(R, \epsilon)$  is directly determined by optical interferometric experiments, it being equal to a stationary optical phase. We therefore refer to  $Y^\beta$  as the "phase function."

Differentiating Eq. (5) with respect to  $R = \kappa_T^{-1/\gamma}$  yields

$$\left( \frac{\partial \ln Y}{\partial \ln R} \right)_\epsilon = W(\theta). \quad (7)$$

Making use of the homogeneity of  $Y$ , i.e.,  $Y(R, \epsilon) = RY(1, \theta)$ , Eq. (7) may be readily integrated to yield  $Y$  when  $W(\theta)$  is known:

$$\ln Y(R, \epsilon) = \ln Y_0 + \ln R + \int_0^\theta \frac{1 - W(\theta')}{\theta'} d\theta', \quad (8)$$

where  $Y_0 = Y(1, 0)$  is an independent constant. Expression (8) is the central result of the present parametric representation. Knowledge of the function  $W(\theta)$  determines the scaled equation of state up to an integration constant.

We are thus led to consider thermodynamic functions on the  $R$ - $\epsilon$  plane, the geometry of which is depicted in Fig. 1. The physical region lies above straight lines which define the minimum inverse compressibility above and below  $T_c$ , and which are loci of  $\mu = 0$ . The lines are  $\epsilon = R\theta_x$ , the critical isochore, and  $\epsilon = R\theta_0$ , the boundary of coexisting phases. The critical point is mapped into the vertex, and straight lines radiating from the vertex are loci of constant  $\theta$ . The critical isotherm is thus also an iso- $\theta$ , i.e.,  $\theta = 0$ .

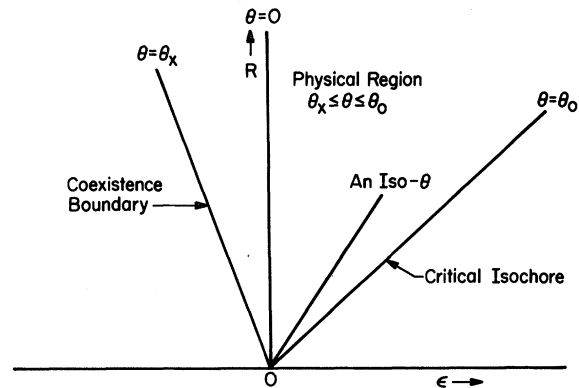


FIG. 1.  $R$ - $\epsilon$  plane, where  $R = \kappa_T^{-1/\gamma}$  and  $\epsilon = (T - T_c)/T_c$ . The physical region lies between the coexistence boundary ( $\theta = \theta_x$ ) and the critical isochore ( $\theta = \theta_0$ ). Scaling implies that thermodynamic quantities are smooth functions of  $\theta$  for fixed  $R$ , with critical singularities being manifest as  $R \rightarrow 0$ .

Based upon quite general properties of  $\mu$  vs  $\rho$  along isotherms near  $T_c$ , and making use of the defining relation Eq. (6), necessary properties of the function  $W(\theta)$  may be derived<sup>5</sup>:

$$\text{Coexistence boundary: } W(\theta_x) = 0; \quad (9a)$$

$$\text{Critical isotherm: } W(0) = 1; \quad (9b)$$

$$\text{Critical isochore: } W(\theta_0) \rightarrow \infty. \quad (9c)$$

An obvious choice, which we call the "W hypothesis," is the bilinear form

$$W(\theta) = \frac{1 - \theta/\theta_x}{1 - \theta/\theta_0}. \quad (10)$$

This function satisfies the physical constraints, Eqs. (9), and contains no other obvious features. Integration of this expression according to Eq. (8) yields the phase function

$$Y(R, \epsilon) = Y_0 R(1 - \theta/\theta_0)^\Delta, \quad (11)$$

where

$$\Delta = 1 - \theta_0/\theta_x. \quad (12)$$

Expression (11) is the parametric equation of state resulting from the  $W$  hypothesis. All thermodynamic functions may be expressed in terms of  $Y(R, \epsilon)$  and  $W(\theta)$ , according to Eqs. (1)–(3). The phase function, Eq. (11), relates (as will be shown) stationary optical phase, isothermal compressibility, and temperature in a form involving six parameters:  $\beta$ ,  $\gamma$ ,  $T_c$ ,  $Y_0$ ,  $\Delta$ , and  $\theta_0$ . The closest contact with this representation is provided by the work of Ho and Litster,<sup>10</sup> who have proposed a five-parameter transformation in which magnetic susceptibility is independent of the scaled variable  $\theta$ . If the parameter combination  $\beta\Delta$  is fixed at the value  $\frac{3}{2}$ , the  $W$ -hypothesis identically reproduces the Ho-Litster representation (see Appendix B). We know of no *a priori* reason why  $\beta\Delta$  should be so fixed, and therefore prefer to allow  $\Delta$  to be a free parameter.

### III. THE INTERFEROMETRIC EXPERIMENT

#### A. Introduction

As the critical point is approached in a pure fluid, the isothermal compressibility increases rapidly, so that in a typical experiment  $\kappa_T$  may be a million times larger than the compressibility of a corresponding ideal gas. In a gravitational field, this effect is manifested by a noticeable compression of the fluid under its own weight, and in equilibrium the fluid is characterized by an inhomogeneous density distribution  $\rho(z, T)$ , where  $z$  denotes height in the fluid. Conventional  $PVT$  measurements, which determine average density and pressure in a macroscopic volume, are thus

bound to fail when  $\rho(z, T)$  varies appreciably over the height of the sample.

Of the several methods which have been devised to circumvent this difficulty, optical techniques appear to be the simplest and most precise. In the present work we have employed an optical interferometric technique developed by Wilcox and Balzarini.<sup>8,9</sup> A quite similar method was originally proposed by Gouy<sup>11</sup> and subsequently applied by several experiments<sup>12-14</sup> to the study of diffusion rates in binary mixtures.

#### B. The interferometric technique

We consider a sample of single-component dielectric fluid compressed in a vessel with plane-parallel optical windows, such that the average density  $\bar{\rho}$  closely approximates the critical density. If the sample temperature is held constant, then due to gravity an equilibrium density distribution,  $\rho(z, T)$ , is formed. The general shape of this distribution for  $T > T_c$  and  $T < T_c$  is depicted in Fig. 2. The discontinuity for  $T < T_c$  indicates the liquid-gas interface (meniscus) characteristic of coexisting phases.

In thermal equilibrium, the chemical potential everywhere in the fluid must be constant. At any point, the total chemical potential consists of the local chemical potential  $[\partial A(\rho, T)/\partial \rho]_T$ , plus a term  $gz$ , the potential energy per unit mass due to gravity. Thus the difference in local chemical potential between points of different densities is proportional to the height difference  $\Delta z$ . Denoting by  $z_0$  the height at which the critical density occurs, we have for the reduced chemical potential difference ( $\mu^* = \mu$ )

$$\mu = -(z - z_0)/h, \quad (13)$$

where  $h = P_c/\rho_c g = 5.412 \times 10^4$  cm for xenon. Thus, height and chemical potential are proportional quantities in fluid experiments, and a knowledge

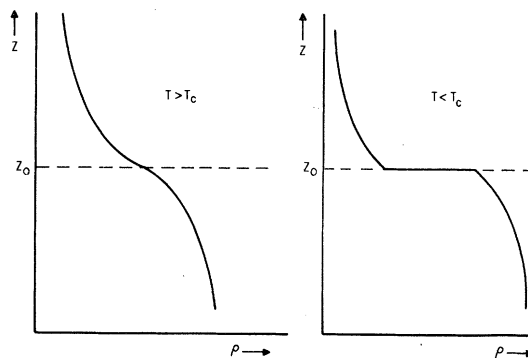


FIG. 2. Schematic illustration of the equilibrium density distribution  $\rho(z, T)$  for  $T > T_c$  and  $T < T_c$ . The discontinuity for  $T < T_c$  indicates the meniscus which characterizes the two-phase region.

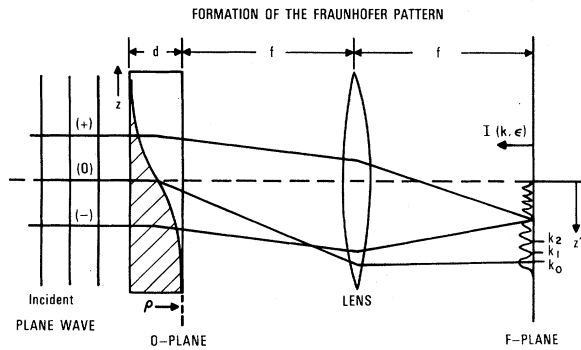


FIG. 3. Simple ray diagram illustrating formation of the Fraunhofer interference pattern from a vertical slab of fluid. Such a diagram is a geometric means of visualizing the stationary-phase approximation to the Fraunhofer integral.

of the distribution  $\rho(z, T)$  for all temperatures would amount to a determination of the equation of state.

The optical cell is illuminated by a suitably expanded beam of monochromatic plane-wave light from a laser (He-Ne,  $\lambda = 6328$  a.u.). In the focal plane of an objective lens placed after the cell, a Fraunhofer interference pattern is observed, characteristic of the density distribution  $\rho(z, T)$  of the fluid phase object. In Fig. 3 we illustrate the formation of the Fraunhofer pattern, based on a simple ray picture. A ray bundle traversing the fluid at height  $z$  is refracted downward through an angle proportional to the density gradient  $\partial\rho/\partial z$ . The ray labeled (0), which is most strongly re-

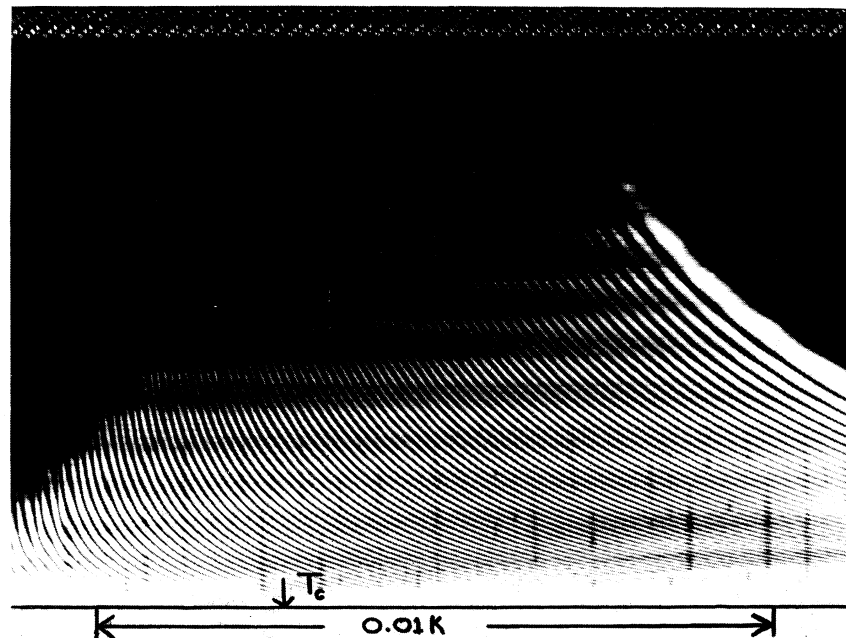
fracted, passes through the region where the critical density occurs, and is focused at the point  $k_0$  in the  $F$  plane. Above and below the maximum gradient are shown a general ray pair (+) and (-) which are refracted through equal angles and hence focused to a common point  $k$  in the  $F$  plane. These rays are in general out of phase, having passed through different fluid densities, so that a series of interference fringes is formed.

Placing a photographic film in the  $F$  plane and slowly transporting it past the pattern (perpendicular to the plane of Fig. 3) while simultaneously sweeping the sample temperature, results in a photograph such as that shown in Fig. 4, which displays the Fraunhofer pattern from a sample of xenon, as a function of temperature. This particular record spans a range of  $\sim 0.02$  K around  $T_c$ , sweeping temperature at a rate of  $\sim 0.8$  mK/h. As will be argued in the remainder of this section, such an intensity distribution  $I(k, \epsilon)$  is determined by the equation of state in the near-critical region.

Several qualitative features of Fig. 4 may be noted. Any narrow vertical slice represents  $I(k, \epsilon)$  at a particular temperature. The critical temperature is associated with no particular feature of the pattern, which proceeds smoothly through  $T_c$  with no apparent discontinuity. For  $T > T_c$ , the most refracted maximum, corresponding to the ray bundle (0) in Fig. 3, is a measure of the density gradient  $\partial\rho/\partial z$  [and hence the isothermal compressibility, by Eq. (13)] on the critical isochore.

For subcritical temperatures the pattern is observed to disappear, beginning with the lowest-

FIG. 4.  $F$ -plane intensity distribution  $I(k, T)$  from a sample of xenon. This sweep took about 24 h. Divergence of fringes for  $T \rightarrow T_c^+$  reflects the diverging isothermal compressibility; disappearance of fringes for  $T < T_c$  indicates a density discontinuity, i.e., the coexistence boundary. Any fringe, maximum, or minimum, is a locus of constant optical phase.



order fringes. This effect is associated with the formation of a discontinuity,  $\rho_L - \rho_G$ , in the density distribution for  $T < T_c$ , and hence a discontinuity  $\Delta\phi$  in optical phase. Thus,  $\Delta\phi$  is the minimum phase difference between rays passing just above and just below the meniscus, and fringes corresponding to a phase difference less than  $\Delta\phi$  must have passed out of the cell. By counting fringes and noting when they vanish, one obtains a measure of the discontinuity as a function of temperature, which is directly related to the fluid coexistence curve.

### C. The Fraunhofer integral

Upon traversing the fluid slab, the incident plane wave is phase shifted. The field immediately after transmission is given by

$$E(z) = f(z)e^{i\phi(z)}. \quad (14)$$

The real factor  $f(z)$  accounts for attenuation of the beam due to opalescent scattering, the strength of which depends on density and hence on height in the fluid. In the ensuing discussion,  $f(z)$  will be assumed to be slowly varying, since we shall be concerned only with zeros of the Fraunhofer pattern.

The phase factor  $\phi(z)$ , relative to  $z_0 = 0$ , depends upon the refractive index  $n(z)$ , according to

$$\phi(z) = (2\pi d/\lambda)[n(z) - n_c], \quad (15)$$

where  $d$  is the window spacing and  $n_c$  the refractive index at  $\rho = \rho_c$ . The fluid density and refractive index are related by the Lorentz-Lorenz formula:

$$(n^2 - 1)/(n^2 + 2) = A\rho, \quad (16)$$

where  $A = \text{constant}$ . (In this expression,  $\rho$  refers to the true number density, not the reduced density  $\rho^*$ .) Expanding Eq. (16) in a Taylor series around  $\rho = \rho_c$ , we obtain

$$n(z) - n_c = (n_c - 1)a_1[\rho + a_2\rho^2] + \dots, \quad (\rho = \rho^*) \quad (17)$$

where

$$a_1 = (n_c + 1)(n_c^2 + 2)/6n_c, \\ a_2 = (n_c^2 - 1)(3n_c^2 - 2)/12n_c^2.$$

For xenon these constants have the values:  $a_1 = 1.03$ ,  $a_2 = 0.04$ , using  $n_c = 1.1379$ .<sup>15</sup> Thus, to first order in reduced density, we have

$$\phi(z) = \alpha\rho(z), \quad (18a)$$

with

$$\alpha = (2\pi d/\lambda)a_1(n_c - 1). \quad (18b)$$

In the present experiments, the fluid density varies only  $\pm 10\%$  from  $\rho_c$ , so that the quadratic term in the expansion (17) may be safely neglected.

In deriving Eq. (18) we have assumed the Lorentz-Lorenz formula to be valid arbitrarily close to the critical point. It is evident that this relationship must fail when the correlation length  $\xi$  associated with coherent long-range density fluctuations becomes comparable with the optical wavelength. Using light scattering, Giglio and Benedek<sup>16</sup> have found that  $\xi = \xi_0\epsilon^{-\nu}$ , with  $\xi_0 = 1.8$  a.u. and  $\nu = 0.57$ , for xenon. On the basis of this result, we may expect that  $\lambda/\xi \approx 1$  when  $\epsilon \approx 6 \times 10^{-7}$ . This temperature is smaller by a factor of  $\sim 10$  than the temperature resolution attained in the present work. Measurements by Hocken<sup>17</sup> of the phase shift of light passing vertically through a thin slab of xenon show that the average refractive index is constant to within  $\sim 6$  parts in  $10^4$ , in the range  $-10^{-4} < \epsilon < 10^{-4}$ . The effect of such a variation is smaller than the neglect of the quadratic term in the Taylor expansion, Eq. (17).

The field  $V(k, T)$  in the  $F$  plane is related to the field  $E(z)$ , Eq. (14), by the Fourier integral

$$V(k, T) = \int_{\text{bottom}}^{\text{top}} e^{i[\phi(z, T) + kz]} dz, \quad (19)$$

where  $k$  is the spatial frequency, given by (see Fig. 3)

$$k = (2\pi/\lambda)z'/f. \quad (20)$$

The  $F$ -plane intensity is just  $I(k, T) = |V(k, T)|^2$ . In writing Eq. (19), we have omitted the slowly varying attenuation factor  $f(z)$ . With expressions (13) and (18) for the reduced chemical potential and phase shift, the Fraunhofer integral becomes

$$V(k, T) = -h \int_0^{\mu_{\text{max}}} \cos(\alpha\psi) d\mu, \quad (21)$$

where the optical phase  $\psi = \psi(\mu, k, T)$  is given by

$$\psi(\mu, k, T) = \rho - hk\mu/\alpha. \quad (22)$$

The form of expression (21) reflects the explicit assumption of exact antisymmetry of  $\mu$  vs  $\rho$  along isotherms, which is inherent in theoretical models such as the lattice gas, and which is apparently a property of real fluids as well, for  $|\rho| \lesssim 30\%$ .<sup>18</sup>

In Fig. 5 we depict the general behavior of the optical phase  $\psi$ , as a function of  $\mu$ , for a particular (supercritical) temperature  $T$  and spatial frequency  $k$ . The principal contribution to the integral Eq. (21) comes from the region  $\mu_+(k, T)$  where the phase is stationary. Accordingly, we calculate

$$\left(\frac{\partial\psi}{\partial\mu}\right)_T = \left(\frac{\partial\rho}{\partial\mu}\right)_T - \frac{hk}{\alpha} = \kappa_T - \frac{hk}{\alpha}, \quad (23)$$

where  $\kappa_T = (\partial\rho/\partial\mu)_T$  is the (dimensionless) isothermal compressibility. At the stationary point

$\mu_+(k, T)$ , the derivative Eq. (23) vanishes, so that

$$k = (\alpha/h)\kappa_T. \quad (24)$$

The value of the phase at the stationary point is then

$$\psi_+ = \psi(\mu_+, (\alpha/h)\kappa_T, T) = \rho_+ - \kappa_T\mu_+, \quad (25)$$

where  $\rho_+ = \rho(\mu_+, T)$ . Then, as a first approximation to the Fraunhofer integral, one might directly replace  $\psi$  by  $\psi_+$  in Eq. (21), so that

$$V(k, T) \propto \cos \alpha\psi_+. \quad (26)$$

The zeros of the  $F$ -plane intensity distribution  $I(k, T)$  would then correspond to the roots

$$\alpha\psi_+ = (2S-1)\pi/2, \quad S=1, 2, \dots \quad (27)$$

This is just the elementary stationary-phase approximation.

#### D. The cubic approximation

The elementary approximation given by Eq. (26) may be improved by noting that the phase  $\psi(\mu)$  in Fig. 5 resembles a cubic function of  $\mu$ . With this suggestion, we introduce a new variable  $\eta$ , defined implicitly for fixed  $k$  and  $T$  by

$$\psi(\mu) = -\frac{1}{3}(\eta^3 - \xi\eta) \quad (28a)$$

$$\equiv P(\eta, \xi), \quad (28b)$$

where

$$\xi \equiv (\frac{3}{2}\psi_+)^{2/3}. \quad (28c)$$

The cubic polynomial  $P(\eta, \xi)$  is stationary at  $\eta_+ = \sqrt{\xi}$  (we are concerned only with positive  $\eta$ ), with the stationary value given by

$$P_+ = P(\sqrt{\xi}, \xi) = \psi_+. \quad (29)$$

With the definition (28), the Fraunhofer integral becomes

$$V(k, T) = -h \int_0^{\eta_{\max}} \cos[\alpha P(\eta, \xi)] \left(\frac{d\mu}{d\eta}\right) d\eta. \quad (30)$$

This expression is still exact; we have merely made a change of variable. To the extent that the factor  $(d\mu/d\eta)$  is slowly varying, we may approximate it by its value at the stationary point. Then, formally extending the upper limit of integration to infinity, we obtain

$$\begin{aligned} V(k, T) &= -h \frac{d\mu}{d\eta} \Big|_{\sqrt{\xi}} \int_0^{\infty} \cos[\alpha P(\eta, \xi)] d\eta \\ &= \text{const} \times \text{Ai}(-\xi'), \end{aligned} \quad (31)$$

where  $\text{Ai}(-\xi')$  is the Airy function<sup>19</sup> of the variable  $\xi' = \alpha^{2/3}\xi$ . In the lowest cubic approximation, then,

the  $F$ -plane interference minima are associated with the zeros  $\xi'_s$  of the Airy function. These roots have been tabulated.<sup>20</sup> For large  $s$  ( $s \geq 5$ ), they are given by

$$\xi'_s = [\frac{3}{2}\alpha(\psi_+)_s]^{2/3} = [3\pi(4s-1)/8]^{2/3}, \quad (32)$$

so that

$$\alpha(\psi_+)_s = (2s - \frac{1}{2})\pi/2. \quad (33)$$

(For  $s=1$ , formula (32) errs by only 0.8% as compared with the tabulated value. This error decreases rapidly with increasing  $s$ .)

We have considered<sup>21</sup> the perturbations of the Airy-function zeros due to the amplitude factor  $(d\mu/d\eta)$ . Corrections are found to be less than 0.2%.

In the interferometric method, then, experimental data are collected according to the following scheme:

(a) Photograph the Fraunhofer interference pattern  $I(k, T)$  at a fixed supercritical temperature  $T$ , far enough above  $T_c$  so that the first maximum is visible.

(b) Assign order numbers  $s=1, 2, \dots$  to the interference minima [zeros of  $I(k, T)$ ], beginning with the most-refracted minimum.

(c) Measure the refraction angles  $k_s$  of the numbered minima, and assign values to the isothermal compressibility according to Eq. (24).

(d) Assign values to the stationary optical phase  $\psi_+ = \rho - \kappa_T\mu$  of each minimum, using tabulated zeros of the Airy function [or Eq. (33) for large  $s$ ].

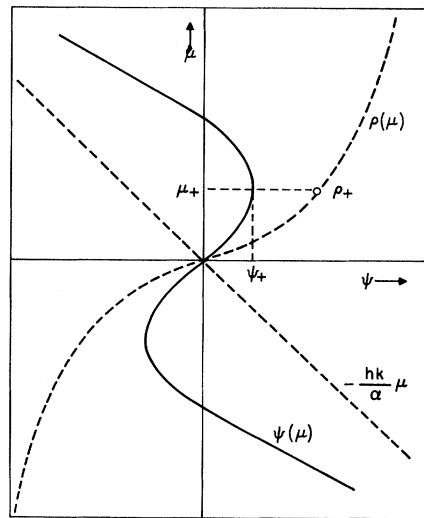


FIG. 5. Optical phase  $\psi(\mu)$  for a general supercritical temperature,  $T > T_c$ . The similarity of  $\psi(\mu)$  to a cubic function leads to the Airy-function approximation to the Fraunhofer integral.

(e) Lower the temperature to a new equilibrium value, photographing continuously so that the minima may be tracked and order numbers assigned unambiguously.

(f) Repeat the measurements of (b)–(e).

The optical experiment thus yields the data pairs  $[\psi_s = \rho - \kappa_T \mu, \kappa_T = (\partial \rho / \partial \mu)_T]$  for fixed  $T$ . In the language of the parametric representation described in Sec. II, we measure  $Y^\beta(R, \epsilon)$ ,  $R^\gamma$ , and  $T$ .

#### IV. RESULTS

##### A. Coexistence curve

In the interferometric experiment, the formation of a density discontinuity,  $\rho_L - \rho_G$ , for subcritical temperatures, is manifested by the disappearance of interference fringes from the Fraunhofer pattern. We consider an interference minimum labeled by an order number  $S$ , with  $S=1$  denoting the first (most-refracted) minimum. According to the stationary-phase approximation, this fringe is formed by two rays which traverse the fluid above and below the point of maximum gradient, and arrive at a common point in the  $F$  plane with a phase difference given by

$$\Delta\phi_s = (2S-1)\pi. \quad (34)$$

Tracking this fringe continuously, we observe that it is refracted out of the cell at a subcritical temperature  $T_s$ , at which point the two rays lie just above and just below the meniscus. The phase difference  $\Delta\phi_s$  then measures the discontinuity  $n_L - n_G$  in the refractive index, according to

$$\Delta\phi_s = kd\Delta n = (2\pi d/\lambda)(n_L - n_G), \quad (35)$$

where  $d$  is the cell thickness. With Eq. (17), we

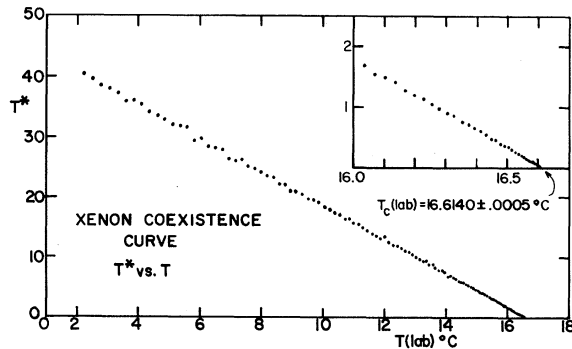


FIG. 6.  $T^* = -(d \ln \Delta \rho^* / dT)^{-1}$  vs  $T$  from numerically differentiated coexistence-curve data. The critical temperature is determined from the extrapolated  $T$ -axis intercept.

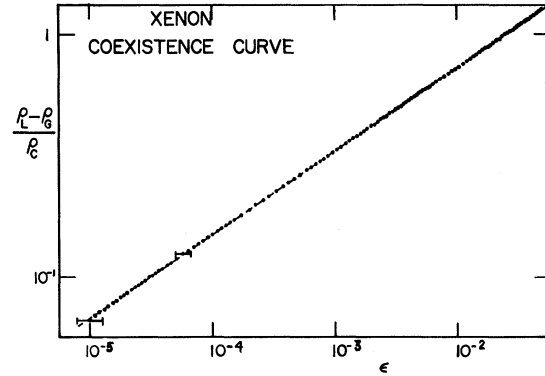


FIG. 7. Xenon coexistence curve  $(\rho_L - \rho_G) / \rho_c$  vs  $\epsilon$ . Error bars include effects of measurement error and uncertainty in  $T_c$ .

then have for the density difference

$$\Delta\rho^* = (\rho_L - \rho_G) / \rho_c = (\lambda / 0.284d)(2S-1). \quad (36)$$

In the present experiment we have counted fringes up to  $S \approx 1500$ , over the temperature range  $10^{-5} < |\epsilon| < 5 \times 10^{-2}$ .

In order to determine  $T_c$ , we numerically differentiate the data according to Kouvel and Fisher,<sup>22</sup> and calculate the quantity

$$T^*(T) = -\left(\frac{d \ln \Delta \rho^*}{dT}\right)^{-1}. \quad (37)$$

In Fig. 6 are plotted experimental values of  $T^*(T)$  vs temperature. The points for  $\Delta T < 0.6$  K ( $\epsilon < 10^{-3}$ ) are then fitted by a linear least-squares program, with the critical temperature determined by the  $T$ -axis intercept.

After determination of  $T_c$ , we plot  $\Delta\rho^*$  vs reduced temperature  $\epsilon$ . The results are shown in Fig. 7. The error bars reflect an estimated uncertainty of  $\pm 0.0005$  K in  $T_c$ . The data are then fitted by the asymptotic form

$$\Delta\rho^* = (\rho_L - \rho_G) / \rho_c = B(-\epsilon)^\beta \quad (38)$$

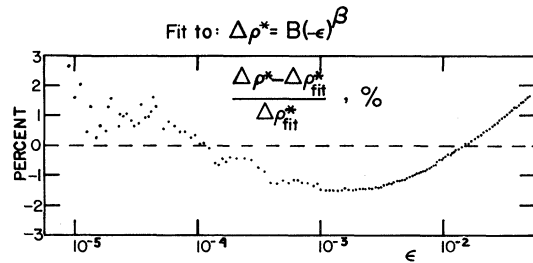


FIG. 8. Deviation plot resulting from fit of coexistence data to  $\Delta\rho^* = B(-\epsilon)^\beta$ . Strongly systematic behavior is clearly evident, suggesting corrections to asymptotic behavior.

while varying the range of  $\epsilon$ . The results are

(a) All data,  $10^{-5} < |\epsilon| < 5 \times 10^{-2}$ :

$$\beta = 0.344 \pm 0.003,$$

$$B = 3.51 \pm 0.05;$$

(b) Range  $|\epsilon| < 10^{-3}$ :

$$\beta = 0.337 \pm 0.003,$$

$$B = 3.30 \pm 0.02;$$

(c) Range  $|\epsilon| > 10^{-3}$ :

$$\beta = 0.353 \pm 0.001,$$

$$B = 3.66 \pm 0.004;$$

(d) Range  $|\epsilon| > 10^{-2}$ :

$$\beta = 0.357 \pm 0.001,$$

$$B = 3.713 \pm 0.002.$$

The quoted standard deviations result almost entirely from uncertainty in  $T_c$ . The tendency of the exponent  $\beta$  to increase with increasing  $|\epsilon|$  is strikingly revealed by the deviation plot, Fig. 8, where we display the deviations  $(\Delta\rho^* - \Delta\rho_{\text{fit}}^*)/\Delta\rho_{\text{fit}}^*$  vs  $\epsilon$ , using

$$\Delta\rho_{\text{fit}}^* = 3.51(-\epsilon)^{0.344}. \quad (39)$$

The marked systematic behavior of the deviations in Fig. 8 indicates that the simple power law, Eq. (38), is not sufficient to describe the coexistence boundary over an extended range in  $\epsilon$ . Wilcox and Balzarini<sup>9,9</sup> have considered the effect of the slope of the rectilinear diameter and a non-constant Lorentz-Lorenz function  $(n^2 - 1)/(n^2 + 2)$ , and have concluded that the resultant uncertainty in the exponent  $\beta$  is  $\pm 0.001$  due to these corrections.

We then fit experimental data to the form

$$\Delta\rho^* = B(-\epsilon)^\beta + A(-\epsilon)^{\beta'}, \quad (40)$$

with the result

$$B = 3.042 \pm 0.03, \quad \beta = 0.332 \pm 0.001,$$

$$A = 0.93 \pm 0.04, \quad \beta' = 0.61 \pm 0.02.$$

The resultant deviation plot is shown in Fig. 9. Systematic errors are significantly reduced by addition of the correction term. Both fits of coexistence data are unweighted ( $1/\sigma^2 = 1$  for each point); addition of the correction term in Eq. (40) reduces the weight  $= 1/\chi^2$  by a factor of 2.1, for 161 points.

#### B. Supercritical compressibility

In the interferometric experiment, the maximum spatial frequency  $k_0$  (see Fig. 3) is a measure of the isothermal compressibility on the critical iso-

chore. From Eq. (24), we have

$$\kappa_T = P_c K_T = h k_0 / \alpha, \quad \rho = \rho_c, \quad (41)$$

where  $\alpha = (2\pi/\lambda)(1.03)(n_c - 1)$ ,  $h = P_c/\rho_c g$ , and  $K_T$  is the unreduced compressibility. In writing this expression we have explicitly inserted a factor  $P_c$  which makes the left-hand side dimensionless.

In the present work we have measured the supercritical compressibility over the temperature range  $2.7 \times 10^{-5} < \epsilon < 4 \times 10^{-2}$ . The data are shown in Fig. 10. Employing holographic techniques to cancel window distortions (see Sec. VD), refraction angles are measured down to the diffraction limit defined by the cell aperture (2 cm).

The data are fitted by the power law

$$P_c K_T = \Gamma \epsilon^{-\gamma} \quad (42)$$

using a weighted least-squares program. Each point is weighted according to the variance

$$\sigma_{\text{total}}^2 = \frac{\sigma_k^2}{k^2} + \frac{\gamma^2 \sigma_T^2}{(\Delta T)^2}.$$

Temperature errors are estimated to be  $\sigma_T \approx 0.001$  K, while errors in angle measurement are individually assigned to each point, depending on the magnification of the optical system. We again perform the fit while varying the range of  $\epsilon$ , with the result:

(a) All data,  $10^{-5} < \epsilon < 10^{-1}$ :  $\gamma = 1.26 \pm 0.002$ ,

$$\Gamma = 0.056 \pm 0.001;$$

(b) Range  $\epsilon < 10^{-3}$ :

$$\gamma = 1.232 \pm 0.006,$$

$$\Gamma = 0.073 \pm 0.005.$$

The observed tendency of the exponent  $\gamma$  to increase for large  $\epsilon$  is reflected in the deviation plot, Fig. 11, where we display the deviations

$$[(P_c K_T)^{-1} - (P_c K_T)_{\text{fit}}^{-1}] / (P_c K_T)_{\text{fit}}^{-1}$$

as a function of  $\epsilon$ . In analogy with the treatment of coexistence-curve data, we then assume a cor-

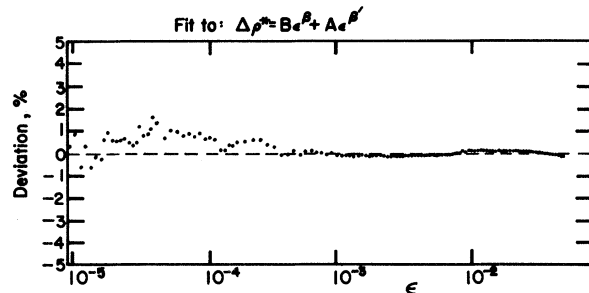


FIG. 9. Deviation plot resulting from fit of coexistence data to a modified power law. Systematic deviations are greatly reduced, with  $\beta'$  surprisingly close to  $2\beta$ .

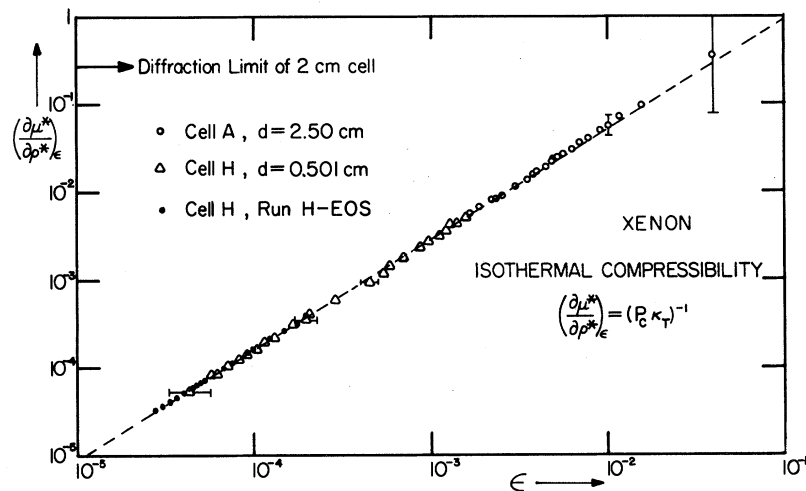


FIG. 10. Supercritical compressibility  $P_c K_T$  vs  $\epsilon$  along the critical isochore of xenon. Holographic techniques allow cancellation of optical distortions, so that refraction angles may be measured down to the diffraction limit.

rection term to the asymptotic power law, fitting data by the form

$$P_c K_T = \Gamma \epsilon^{-\gamma} + C \epsilon^{-\gamma'}, \quad (43)$$

holding  $\gamma = 1.230$ . [Allowing both  $\gamma$  and  $\gamma'$  to be free parameters causes no end of confusion for the computer.] With Eq. (43) for the fitting function, the result is:

All data,  $10^{-5} < \epsilon < 10^{-1}$ :  $\Gamma = 0.0503 \pm 0.009$ ,  
 $\gamma = 1.230$ , fixed,  
 $C = 0.0079 \pm 0.007$ ,  
 $\gamma' = 1.35 \pm 0.07$ .

In traversing the fluid sample, light which forms the most refracted fringe necessarily passes through a range of densities around  $\rho_c$ . As  $T - T_c$ , this effect causes the spatial frequency  $k_0$  to differ from the result predicted by the stationary-phase approximation. Wilcox and Balzarini<sup>8,9</sup> have calculated the effect on experimental data of a breakdown of this "thin-cell approximation." We are

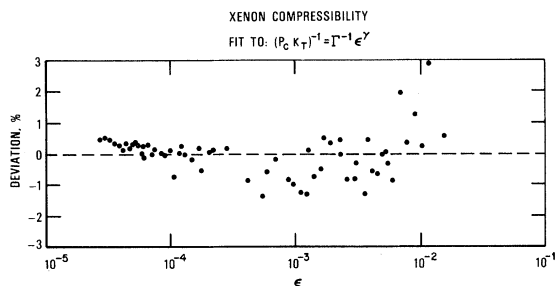


FIG. 11. Deviation plot for isothermal compressibility data, indicating a slight tendency for  $\gamma$  to decrease with decreasing  $\epsilon$ . A fit to a modified power law yields a result which is not statistically significant.

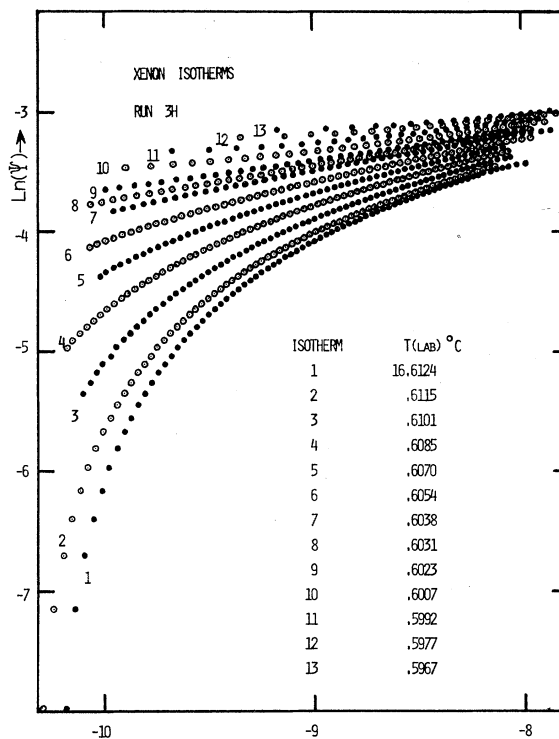


FIG. 12. Plot of  $\ln \psi_+$  vs  $\ln(1/\kappa_T)$  along isotherms of xenon. According to the static hypothesis, supercritical isotherms should curve downward and approach infinite slope as  $\theta \rightarrow \theta_0$  ( $\ln Y^\beta \rightarrow -\infty$ ). Subcritical isotherms curve upward and approach zero slope at the coexistence boundary,  $\theta = \theta_x$ . The critical isotherm is characterized by a constant slope  $\beta/\gamma$ . Visual inspection reveals  $T_c$  to lie somewhere between isotherms No. 8 and No. 9, which are 0.0008 K apart.

thus led to reject compressibility data from cell A for  $\epsilon < 4 \times 10^{-5}$  and from cell H for  $\epsilon < 10^{-5}$ .

### C. The equation of state

#### 1. The critical temperature

In experimental studies of critical phenomena, a precise determination of the critical temperature on a laboratory scale is essential. This is particularly true in an interferometric experiment, since equation-of-state data from the Fraunhofer pattern are generally confined to the temperature range  $-10^{-4} < \epsilon < 10^{-4}$ . Hence even small errors in  $T_c$  may readily affect experimental conclusions. The scaling formulation described in Sec. II suggests a new operational definition of  $T_c$ , assuming the validity of the static scaling hypothesis. In this section we apply this scheme to interferometric data from near-critical isotherms in xenon.

The optical data consists of typically 75 pairs  $\psi_+ = Y^\beta(R, \epsilon)$  and  $\kappa_T = R^{-\gamma}$  for each isotherm both above and below  $T_c$ . From Eq. (7) we derive, in terms of measured quantities,

$$-\frac{d \ln \psi_+}{d \ln \kappa_T} = \frac{\beta}{\gamma} W(\theta), \quad (44)$$

with  $\theta = \epsilon/R = \epsilon \kappa_T^{1/\gamma}$ . Equation (44) suggests plotting experimental data  $\ln \psi_+$  vs  $\ln(1/\kappa_T)$ . The isotherm slope on this plot is  $(\beta/\gamma)W(\epsilon \kappa_T^{1/\gamma})$ , and thus is independent of  $\kappa_T$  only when  $\epsilon=0$ , i.e.,  $T=T_c$ . In Fig. 12 we display experimental isotherms plotted in this manner. This particular data run (3H) consists of some 1200 points from 27 isotherms; for the sake of clarity, only 13 isotherms are plotted in Fig. 12.

For supercritical temperatures, the isotherms curve downward, approaching infinite slope as  $\theta \rightarrow \theta_0$  ( $\ln \psi_+ \rightarrow -\infty$ ). Subcritical isotherms curve upward, tending toward zero slope at an indefinite locus  $\theta \rightarrow \theta_c$ . Close inspection reveals that the critical isotherm, defined according to Eq. (44), lies between the isotherms labeled No. 8 and 9, which

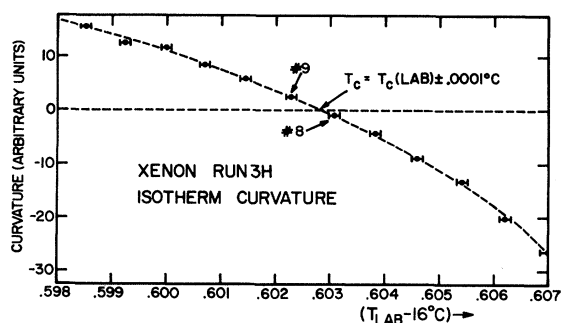


FIG. 13. "Curvature coefficient"  $-\beta a \epsilon$  vs  $\epsilon$  for xenon isotherms. The critical temperature is signalled by the zero crossing of the curvature coefficient.

differ in temperature by 0.8 mK.

To obtain a better estimate of  $T_c$ , we expand the function  $W(\theta)$  in a Taylor series around  $\theta=0$ :

$$W(\theta) = 1 + a\theta + O(\theta^2) \approx 1 + a(\epsilon/R), \quad (45)$$

where  $a = \text{constant}$ . [With the  $W$  hypothesis,  $a = \Delta/\theta_0$ . The present analysis, however, is independent of the choice of  $W(\theta)$ .] Integration of Eq. (45) according to Eq. (8) yields for the phase function near  $\theta=0$

$$\ln Y^\beta(R, \epsilon) = \ln Y_0^\beta + (\beta/\gamma) \ln R^\gamma - \beta a \epsilon \exp[(-1/\gamma) \ln R^\gamma], \quad (46)$$

or, in terms of measured quantities,

$$\ln \psi_+ = \ln Y_0^\beta + (\beta/\gamma) \ln(1/\kappa_T) - \beta a \epsilon \exp[(-1/\gamma) \ln(1/\kappa_T)]. \quad (47)$$

Experimental data pairs  $[\ln \psi_+, \ln(1/\kappa_T)]$  along isotherms are then fitted by the form

$$\ln \psi_+ = A + B \ln(1/\kappa_T) + C \exp[(-1/\gamma) \ln(1/\kappa_T)], \quad (48)$$

using a nonlinear least-squares program. We assume  $\gamma = 1.23$ , but the resultant fit is insensitive to the value of  $\gamma$ . In Fig. 13 we plot the coefficient  $C = -\beta a \epsilon$ , which is a direct indicator of the location of the critical temperature. This "curvature coefficient" is negative for  $T > T_c$  and positive for  $T < T_c$ . Figure 13 clearly indicates that  $T_c$  is bracketed by isotherms No. 8 and 9 of Fig. 12, and interpolation yields  $T_c(\text{lab}) = 16.6028 \pm 0.0001$  K.

We emphasize that this new operational definition of  $T_c$  involves no parameters, no divergences of thermodynamic quantities, and very short interpolations of experimental data. Our closest approach in this work (isotherm No. 8) is  $\Delta T \approx 0.3$  mK. One may in principle go as close to  $T_c$  as thermostat stability and thermometer resolution allow. The new technique appears capable of yielding an especially precise determination of  $T_c$  in a pure fluid.

As a check we add that the value of  $T_c$  obtained from scaling agrees within error with an independent determination by extrapolation of supercritical compressibility in the standard manner. This indicates that the assumption of static scaling inherent in this new formulation is valid. A more general test of scaling is presented in the following section.

#### 2. Test of the static scaling hypothesis

Once the critical temperature is known, a knowledge of the parameter  $\gamma$  is sufficient to completely specify the scaled variable  $\theta$ , and hence to examine directly the validity of the scaling hypothesis

through the relation

$$\frac{d \ln \psi_+}{d \ln \kappa_T} = -\frac{\beta}{\gamma} W(\theta).$$

The function  $W(\theta)$  is not specified apart from the requirements (see Sec. II)

$$W(\theta)_x = 0; \quad W(0) = 1; \quad W(\theta_0) \rightarrow \infty.$$

To this end, experimental data pairs  $[\ln \psi_+, \ln(1/\kappa_T)]$  are numerically differentiated and the quantity  $[d \ln \psi_+ / d \ln(1/\kappa_T)]$  plotted against  $\theta = \epsilon \kappa_T^{1/\gamma}$ , for a particular choice of  $\gamma$ . The results are displayed in Fig. 14. The data consist of approximately 1200 points from 27 isotherms in the range  $-10^{-4} < \epsilon < 10^{-4}$ . The choice  $\gamma = 1.2245$  is the result of a later computer fit.

It is apparent from Fig. 14 that the static scaling hypothesis is well verified for xenon. The experimentally determined function  $W(\epsilon \kappa_T^{1/\gamma})$  fulfills our qualitative expectations, and all data points may be imagined to lie on a single curve. The error bars in the figure represent estimated temperature and refraction-angle variances and errors introduced in the numerical differentiation.

### 3. The phase function

In Sec. II we introduced the  $W$  hypothesis,

$$W(\theta) = \frac{1 - \theta/\theta_x}{1 - \theta/\theta_0}, \quad (49)$$

a simple bilinear form which possesses the obvious and necessary properties for a phenomenological

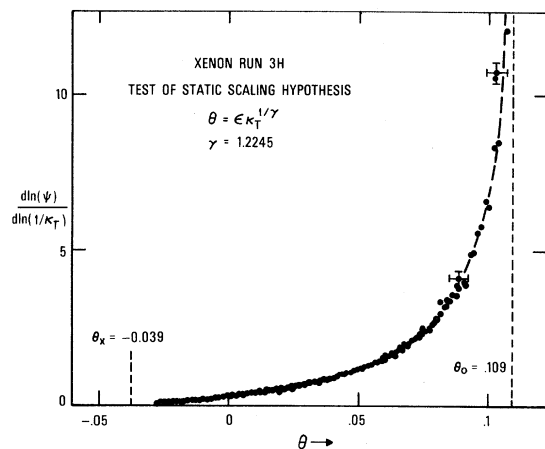


FIG. 14. Quantity  $[d \ln \psi_+ / d \ln(1/\kappa_T)]$  vs  $\theta = \epsilon \kappa_T^{1/\gamma}$  for interferometric data from xenon. The approximately 2000 points may well be imagined to lie on a single curve, which is predicted by the scaling hypothesis. The error bars include the effect of numerically differentiating the data, as well as temperature and angle variances.  $T_c$  was determined from Fig. 13, while the exponent  $\gamma = 1.2245$  resulted from a later computer analysis.

TABLE I. Equation-of-state parameters for xenon. Run 3H; 1176 points.

Parameter	Best-fit value
(a) All parameters free: $\chi^2_0 = 1.14$ ; $\beta\Delta = 1.386 \pm 0.001$	
$\theta_0$	$0.1101 \pm 0.0003$
$Y_0^\beta$	$0.4203 \pm 0.0004$
$\Delta$	$3.869 \pm 0.001$
$\beta$	$0.3583 \pm 0.0002$
$\gamma$	$1.2296 \pm 0.0005$
$T_c$	$16.60301 \pm 0.00004$ °C
(b) Fix $T_c = 16.6028$ °C; $\beta/\gamma = 0.2826$ ; $\chi^2_0 = 1.22$ ; $\beta\Delta = 1.384 \pm 0.001$	
$\theta_0$	$0.1014 \pm 0.0003$
$Y_0^\beta$	$0.3939 \pm 0.0001$
$\Delta$	$3.933 \pm 0.001$
$\beta$	$0.3519 \pm 0.0002$
$\gamma$	$1.2453 \pm 0.0002$
$T_c$	$16.6028$ °C (fixed)
(c) Ho and Litster: $\beta\Delta = 3/2$ ; $\chi^2_0 = 1.71$	
$\theta_0$	$0.1378 \pm 0.001$
$Y_0^\beta$	$0.424 \pm 0.004$
$\Delta$	$4.261 \pm 0.001$
$\beta$	$0.3520 \pm 0.0006$
$\gamma$	$1.203 \pm 0.002$
$T_c$	$16.60304 \pm 0.00002$ °C

description of the gas-liquid transition. The resultant phase function, upon integration of  $W(\theta)$  according to Eq. (8), is given by

$$Y^\beta(R, \epsilon) = Y_0^\beta R^\beta (1 - \theta/\theta_0)^{\beta\Delta}, \quad (50a)$$

with

$$\Delta = 1 - \theta_0/\theta_x. \quad (50b)$$

In terms of experimentally measured quantities  $\psi_+$ ,  $\kappa_T$ , and  $T$ , Eq. (50) becomes

$$\psi_+ = Y_0^\beta \kappa_T^{-\beta/\gamma} \left( 1 - \frac{(T - T_c) \kappa_T^{1/\gamma}}{T_c \theta_0} \right)^{\beta\Delta}. \quad (51)$$

This expression contains six parameters:  $Y_0^\beta$ ,  $\beta$ ,  $\gamma$ ,  $T_c$ ,  $\theta_0$ , and  $\Delta$ . Experimental data are fitted to Eq. (51) and the parameter set determined. The fitting program is a modified general nonlinear least-squares routine known as CURFIT, which has been adapted from Bevington.<sup>23</sup> Temperature and angle measurement errors,  $\sigma_T$  and  $\sigma_k$ , are estimated and used in the fitting program to calculate the statistical variance of each data point, according to

$$\text{Var}\{\psi_+\} = \sigma^2 = \left( \frac{\partial \psi_+}{\partial k} \right)^2 \sigma_k^2 + \left( \frac{\partial \psi_+}{\partial T} \right)^2 \sigma_T^2. \quad (52)$$

If experimental variances are properly assigned,

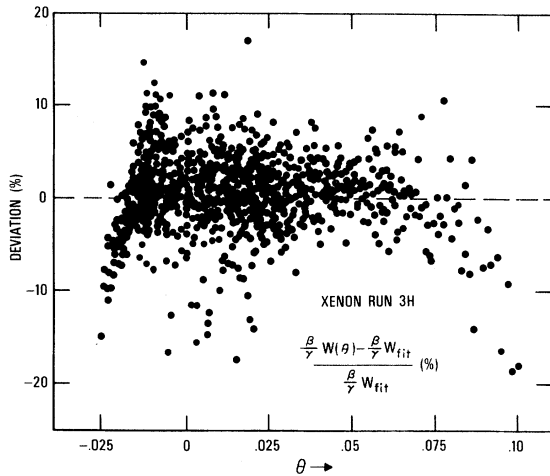


FIG. 15. Deviation plot resulting from a fit of the data of Fig. 14 to the bilinear form introduced in the text. Errors are remarkably small, considering that the data have been differentiated. One can imagine systematic deviations near the endpoints  $\theta = \theta_x$  and  $\theta = \theta_0$ . These presumably result from higher-order terms contributing to  $W(\theta)$ .

the value of  $\chi^2_\nu = [1/(N - \nu - 1)] \sum (\psi_+ - \psi_{+fit})^2$  for a suitable fitting function should be near unity. (Here  $N$  is the number of points and  $\nu$  the number of free parameters.)

The experimental data (run 3H) consist of approximately 1200 pairs  $(\psi_+, \kappa_T)$  from 27 isotherms in the range  $-10^{-4} < \epsilon < 10^{-4}$ . The results of computer analysis are shown in Table I for three modes of fit: (a) all parameters are free, (b)

$\beta/\gamma$  and  $T_c$  fixed at values determined by the technique of Sec. IV C 1, and (c)  $\beta\Delta$  fixed at 1.50, which is equivalent to the representation of Ho and Litster<sup>10</sup> (see Appendix). The standard deviations of the best-fit parameters are remarkably small and are typical for least-squares fits involving a large number of data points. In view of the differences in parameter values in Table I(a) and I(b), these standard deviations should not be considered to be the most accurate indicators of the true uncertainties.

Once the equation-of-state parameters are determined, we may calculate the function

$$\frac{\beta}{\gamma} W_{fit} = \frac{\beta}{\gamma} \frac{1 - \theta/\theta_x}{1 - \theta/\theta_0},$$

which contains five parameters:  $\beta$ ,  $\gamma$ ,  $T_c$ ,  $\theta_0$ , and  $\Delta = 1 - \theta_0/\theta_x$ . In Fig. 15 we display the resultant deviations  $[(\beta/\gamma)W - (\beta/\gamma)W_{fit}]/(\beta/\gamma)W_{fit}$ , using the parameter set of Table III(a). Most scatter is due to the numerical differentiation of the data according to  $d \ln \psi_+ / d \ln(1/\kappa_T) = (\beta/\gamma)W(\theta)$ . The  $W$  hypothesis appears adequate to account for the data. There are possibly systematic deviations near  $\theta_x$  and  $\theta_0$  which could be due to higher-order terms in  $W(\theta)$ . We have not investigated the effects of such corrections.

An attractive means of displaying the data is suggested by rewriting Eq. (51) in the form

$$[\psi_+ \kappa_T^{\beta/\gamma}]^{1/\beta\Delta} = Y_0^{1/\Delta} \left(1 - \frac{\epsilon \kappa_T^{1/\gamma}}{\theta_0}\right). \quad (53)$$

For a suitable parameter set, a plot of the left-hand side of this expression vs  $\kappa_T^{1/\gamma}$  should map

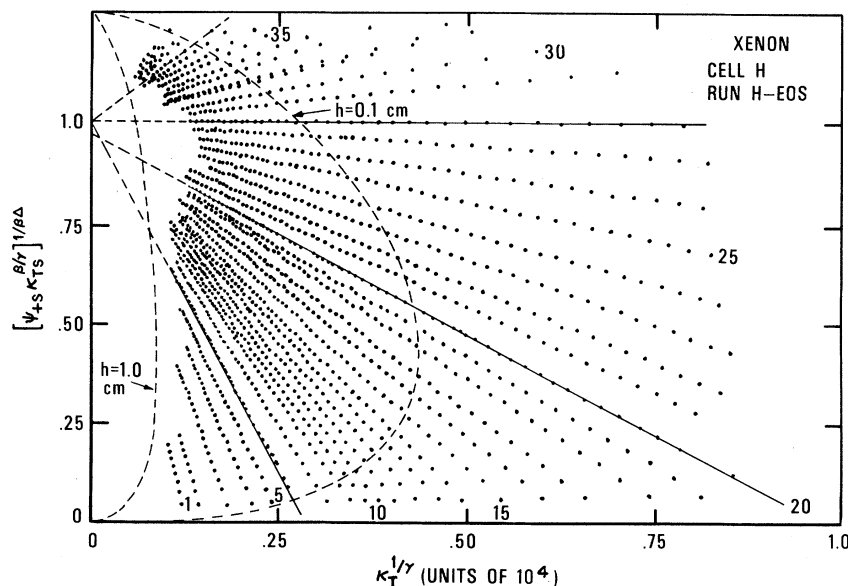


FIG. 16. "Fan plot" of xenon isotherms. Construction of this plot is described in the text. Scaling predicts that isotherms should map into straight lines with slope proportional to  $-\epsilon$ , which is clearly suggested by the data. The fan plot requires five parameters, and is best constructed after fitting the data to an equation of state. The dashed curves are loci of constant  $\mu$  and hence constant height in the gravitational field. Such a locus for  $z=1$  cm defines the minimum compressibility which can be measured in this experiment.

experimental isotherms into straight lines whose slopes are proportional to  $-\epsilon$ . In Fig. 16 are shown 43 xenon isotherms plotted in this manner. This resultant "fan plot" indicates in a striking manner the validity of the scaling hypothesis and in particular the utility of the bilinear  $W$  function, Eq. (49). The dashed curves in Fig. 16 are loci of constant cell height (and hence constant  $\mu$ ) for  $h = 0.1$  and  $1.0$  cm. The latter defines the minimum compressibility  $\kappa_T^{1/\gamma}$  which can be measured in these experiments, determined by the density gradient at the limits of the cell aperture.

In Fig. 17 are shown the slopes of the isotherms in the fan plot, Fig. 16, vs temperature, as determined by least-squares fits. The critical temperature is determined by the zero crossing of the locus of isotherm slopes. We do not advocate this procedure as a means of determining  $T_c$  since construction of the fan plot requires knowledge of three parameters  $\beta$ ,  $\gamma$ , and  $\Delta$ . Also plotted in Fig. 17 are the percentage deviations of the extrapolated intercepts of straight-line fits from the best-fit value  $Y_0^{1/\Delta}$ . These are used only to check experimental data for possible systematic errors.

#### D. Consequences of the scaled equation of state

##### 1. Exponents

Critical exponents play a central role in the phenomenological description of phase transitions. Within the framework of the scaling hypothesis, a knowledge of two critical exponents is sufficient to determine the rest. In the present parametric representation of the scaled equation of state, the exponents  $\beta$  and  $\gamma$  occur in a natural way and are directly determined as phenomenological param-

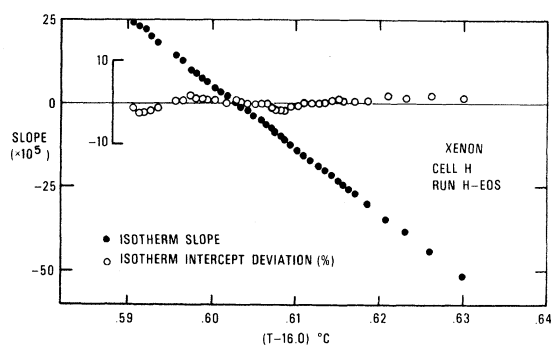


FIG. 17. Isotherm slopes and intercept deviations from the "fan plot" of Fig. 16. These results are used only for consistency checks of experimental data.

TABLE II. Critical exponents resulting from the scaled equation of state. (a) All parameters free. (b)  $T_c = 16.6028$ ,  $\beta/\gamma = 0.2826$ , fixed. (c)  $\beta\Delta = 1.50$ , fixed (Ho and Litster).

Exponent	(a)	(b)	(c)
$\beta$	$0.3583 \pm 0.0002$	$0.3519 \pm 0.0002$	$0.3520 \pm 0.0006$
$\gamma, \gamma'$	$1.2296 \pm 0.0005$	$1.2453 \pm 0.0002$	$1.203 \pm 0.002$
$\delta$	$4.432 \pm 0.001$	$4.539 \pm 0.001$	$4.418 \pm 0.002$
$\alpha, \alpha'$	$0.054 \pm 0.001$	$0.051 \pm 0.001$	$0.093 \pm 0.002$
$\nu, \nu'$	$0.649 \pm 0.001$	$0.650 \pm 0.001$	$0.636 \pm 0.002$
$\eta$	$0.105 \pm 0.01$	$0.083 \pm 0.01$	$0.11 \pm 0.01$

eters. In Table II we tabulate the values of several critical exponents resulting from the best-fit  $\beta$  and  $\gamma$  for each of the three fits of the phase function, Table I.

In the present work, we place particular emphasis on the parameter  $\Delta$  in the form  $\beta\Delta = \beta(1 - \theta_0/\theta_x)$ . In the cubic model of Ho and Litster,<sup>10</sup> this combination takes the value  $\frac{3}{2}$ . We prefer to allow  $\beta\Delta$  to be a free parameter and the result (Table I)  $\beta\Delta = 1.386$  indicates a significant departure from Ho and Litster's restriction.

##### 2. Critical coefficients

When the near-critical equation of state is expressed in parametric form, the critical coefficients of thermodynamic anomalies are directly determined once the parameter set is known.<sup>24</sup> If the supercritical compressibility on the critical isochore and the subcritical compressibility along the coexistence boundary are represented, respectively, by the asymptotic power laws,  $\kappa_T = \Gamma\epsilon^{-\gamma}$  and  $\kappa_T' = \Gamma'(-\epsilon)^{-\gamma'}$  (with  $\gamma = \gamma'$ ), then evidently

$$\Gamma = \theta_0^\gamma, \quad (54)$$

$$\Gamma' = (-\theta_x)^\gamma. \quad (55)$$

The compressibility ratio  $\Gamma/\Gamma'$  is given by

$$\Gamma/\Gamma' = (\Delta - 1)^\gamma. \quad (56)$$

Along the coexistence boundary,  $\theta = \theta_x$ , the reduced density is described by the power law  $\rho = 1/2G(-\epsilon)^\beta$ , whence it follows from Eq. (50) that

$$1/2G = Y_0^\beta (1 - \theta_x/\theta_0)^{\beta\Delta} (-1/\theta_x)^\beta. \quad (57)$$

The critical isotherm,  $\theta = 0$ , is described by  $\mu = C|\rho|^\delta$ , which together with Eqs. (1)–(3) implies

$$C = \frac{\beta/\gamma}{Y_0^\gamma (1 + \beta/\gamma)^\Delta}. \quad (58)$$

In Table III we tabulate the critical coefficients calculated from the fitted parameter sets, Table I.

TABLE III. Critical coefficients calculated from equation-of-state parameters. (a) All parameters free. (b)  $T_c = 16.6028$ ,  $\beta/\gamma = 0.2826$ , fixed. (c)  $\beta\Delta = 1.50$ , fixed (Ho and Litster).

Coefficient	(a)	(b)	(c)
$\Gamma = \theta_0^\gamma$	0.0663	0.0578	0.0922
$\Gamma' = (-\theta_x)^\gamma$	0.0182	0.0151	0.0222
$\Gamma/\Gamma' = (\Delta - 1)^\gamma$	3.654	3.819	4.145
$\frac{1}{2}G$	1.823	1.726	1.687
$C$	1.837	2.468	1.767

## V. EXPERIMENTAL DETAILS

### A. The xenon sample cells

The high-pressure optical cells used in this experiment were constructed on special order by the EIMAC division of Varian Associates. Each consists of a Kovar body, into which sapphire windows of  $\frac{1}{4}$ -in. thickness and  $\frac{3}{4}$ -in. diameter are copper brazed. Although the windows were specified flat to  $\lambda/4$ , distortions are evidently introduced in the brazing process. Further small deformations resulting from high stress ( $\sim 57$  atm) are unavoidable. The subsequent deterioration in optical quality may be remedied through the use of holograms. This technique will be described later in this chapter. Two cells, labeled *A* and *H*, were employed; the respective window spacings are 2.50 and 0.501 cm.

The cells were filled with xenon (Matheson Research Grade: Specified Analysis,  $N_2$  3 ppm, Kr 15 ppm, and  $O_2$  2 ppm) at Columbia University. After baking on a vacuum station at 450 K for eight

hours, to ensure the absence of organic contaminants, the cells were flushed to 1 atm with xenon, flushed again to  $\frac{1}{2}$  atm, and finally filled in a water bath at  $16.2 \pm 0.1$  °C to the half-way mark. One of the cells (*H*) was slightly overfilled, so that the critical density occurred somewhat above the center of the cell. Since the Fraunhofer pattern is invariant under vertical translations in the object plane, the only result of this slight overfilling is a narrow region of uncanceled light in the small-angle portion of the pattern.

### B. The temperature controller

Precise regulation of the sample temperature is required. This is accomplished through the use of a two-stage thermostat. The first stage consists of a cylindrical brass cavity, 12 in. in diameter. Copper cooling coils wound about the cavity carry water thermostatted to  $\pm 0.02$  K by a commercial refrigerated and heated water circulator. Brass face plates, containing optical windows, are fitted to the ends of the cylinder, effecting isolation of the interior from changes in ambient environment. A sensor crystal from a quartz thermometer is embedded in one of the face plates so that the first-stage temperature may be monitored. The entire outer enclosure is insulated with a combination of foam rubber and styrofoam.

The inner thermostat is also cylindrical, and is centered inside the brass cavity, insulated on all surfaces by 2 in. of styrofoam. This stage consists of a massive copper block, 7 in. in diameter, inside of which are clamped the xenon cells and a Ronchi ruling used in angle calibration. This block is accurately machined to accommodate the

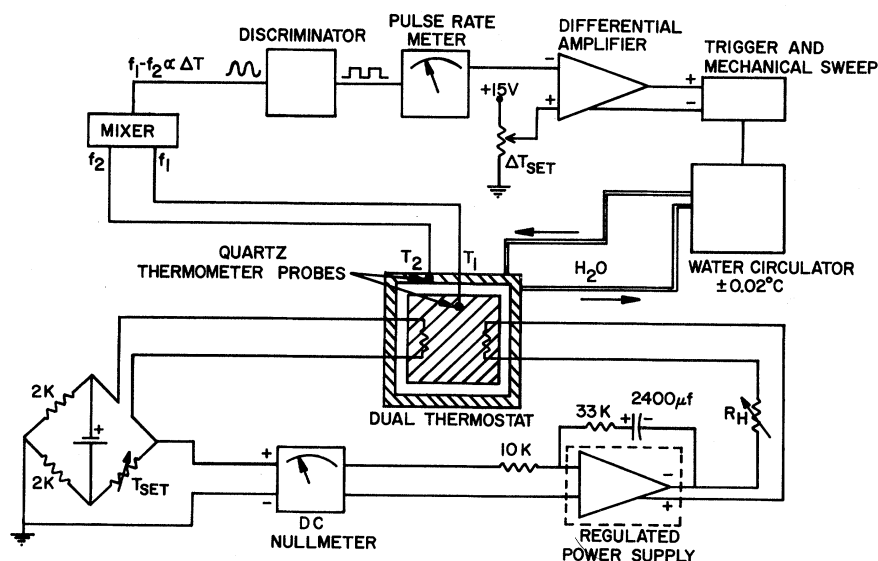


FIG. 18. Schematic diagram of the sample temperature controller. Feedback to the water circulator keeps heater power constant as the set temperature is changed.

cells, which are in firm mechanical contact with the copper. Several thermistors, used for temperature monitoring and control, are sealed into  $\frac{1}{4}$ -20 Allen screws with dental amalgam. These screws are embedded near the center of the copper block, which also contains a quartz-crystal thermometer probe for temperature measurement. The outside of the block is wound with heating wire, used for regulation of the sample temperature.

In Fig. 18 is shown the circuit diagram for the inner temperature controller. One of the thermistors served as an arm of a dc Wheatstone bridge. The error signal from the bridge is amplified by a high-gain dc amplifier, whose output serves as the control input to an operational power amplifier, with combined proportional and integral feedback. The power amplifier supplies current to the heating coils. A precision resistance box (0.01  $\Omega$ /step) allows selection of the desired temperature. It is important to replace the 1.35-V mercury cell in the bridge periodically, in order that the current in the control thermistor be constant. Due to Joule heating, the thermistor rides approximately 30 mK above its environment. A 1.5% change in bridge EMF causes a change in set temperature of about 1 mK.

A beat frequency derived from the quartz crystals in the inner and outer thermostats is counted by a pulse-rate meter, thus providing an analog voltage proportional to the temperature difference,  $T_1 - T_2$ . This voltage is compared to a set voltage by a high-gain differential amplifier, whose output controls a mechanical sweep on the water circulator in on-off fashion, the direction of sweep depending on the polarity of the differential amplifier. With this arrangement, the temperature difference between the two stages is held constant ( $\pm 0.2$  K) as the set temperature is changed. This keeps the required heater power constant, typically less than 50 mW.

It is very important in work of this type to minimize temperature gradients within the sample volume. Although such gradients are nearly impossible to measure accurately to the required sensitivity, they are readily estimated in a conductivity thermostat using the simple expression

$$\frac{\Delta Q}{\Delta t} = \lambda A \frac{\Delta T}{L}.$$

As a worst-case estimate, assuming all heater power (50 mW) applied to one face of the central copper block and exiting through the opposite face, the resultant gradient is 50  $\mu$ K/cm for our experimental geometry. With the cylindrical symmetry actually employed in heating, the gradients must be much smaller than this.

With this thermostat, a set temperature is main-

tained to within 100  $\mu$ K almost indefinitely. Perhaps the most sensitive indicator of thermostat stability is the Fraunhofer pattern from the fluid itself. The most-refracted maximum measures compressibility on the critical isochore, so that the angle  $k_0$  (see Fig. 3) may be expected to diverge as  $T \rightarrow T_c$  according to

$$k_0 = A e^{-\gamma}, \quad A = \text{constant.} \quad (59)$$

From this expression we derive

$$\frac{\Delta k_0}{k_0} = -\frac{\gamma}{T - T_c} \Delta T, \quad (60)$$

which expresses the fractional angle shift resulting from a temperature fluctuation  $T \rightarrow T + \Delta T$ . With the precision film-scanning apparatus employed in these experiments, a change in  $\Delta k_0/k_0$  of (2-3)% is readily measured. Assuming a set temperature 1 mK from critical, with  $\gamma = 1.25$ , then Eq. 60 indicates a temperature sensitivity of about 20  $\mu$ K. Long-term observation of the Fraunhofer pattern at constant temperature indicates the thermostat stability quoted above.

### C. Temperature measurement

The sample temperature within the inner thermostat is measured by a quartz-crystal thermometer (Hewlett-Packard Model No. 2108-A), which has been extensively modified for our purposes. The instrument as received was not suited to the required precision, due to (a) large temperature coefficients ( $\sim 0.001$ -K/K change in ambient temperature) of both the sensor and reference oscillators, and (b) a maximum sampling period of 10 sec, which for a 1-kHz/K sensor crystal leads to temperature roundoff errors of  $\pm 100$   $\mu$ K. These limitations were circumvented as follows.

(a) The 28.208-MHz internal-reference oscillator was replaced with an oscillator of the same frequency, but of much better thermal stability. This consists of a General Radio Type-1164 frequency synthesizer, referenced to a 5-MHz output of a Hewlett-Packard Model No. 107BR quartz oscillator. The frequency stability of this combination is better than 1 part in  $10^{10}$  /K change in ambient temperature, or thermal stability of  $< 5$   $\mu$ K/K ambient. Thermally related fluctuations in the frequency of the sensor oscillator were reduced by enclosure of the oscillator and its probe cable into the inner section of a two-stage cylindrical brass thermostat, where its temperature is controlled to  $\pm 0.01$  K by a thermistor-controlled heater. With this arrangement, observed temperature fluctuations due to the sensor oscillator are reduced to  $< 10$   $\mu$ K.

(b) Round-off errors are reduced by increasing the thermometer sampling period to 1000 sec,

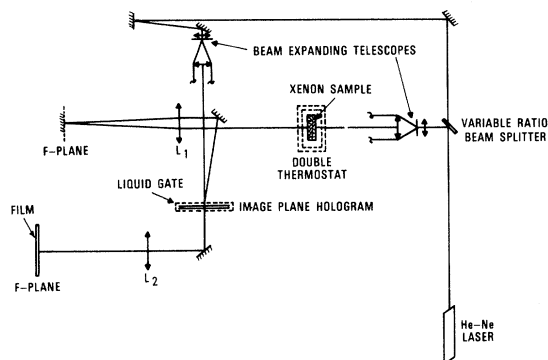


FIG. 19. Schematic diagram of the optical experiment. The "folded" arrangement allows equalizing path lengths when using holograms. For most purposes, the Fraunhofer pattern is photographed directly, in the  $F$  plane behind  $L_1$ .

which is accomplished by inserting a two-decade scaler in the clock circuitry. After each sampling period, the temperature is recorded by photographing the digital output on the film above the interference pattern. In this manner the thermal history of the xenon sample is monitored.

During the course of the equation-of-state run, this modified quartz thermometer aged at a rate of 2 parts in  $10^9$  /h as referenced to both the fluid and to the resistance thermometer.<sup>21</sup> Such frequency aging is always observed in quartz resonators and has been shown to be an exponential function of time.<sup>25</sup> In this experiment, a simple linear correction of 6  $\mu\text{K}/\text{h}$  sufficed to bring the crystal in correspondence with the other thermometers.

#### D. The optical layout

A diagram of the experimental setup is depicted in Fig. 19. The folded optical arrangement allows for matching of path lengths when holographic techniques are employed. For most purposes it suffices to photograph the Fraunhofer pattern directly, placing the film in the  $F$  plane behind lens  $L_1$ . Typical film speeds of 1 in./day are obtained using a modified time-lapse camera (Grass Model No. C4), which is converted to a slow continuous drive.

When measuring very small refraction angles, one becomes limited by the window distortions mentioned in Sec. A above. In these experiments this limitation is avoided using a holographic technique as follows. A photographic plate immersed in a liquid gate (see Fig. 19) is simultaneously illuminated by a focused image of the field after transmission through the cell and a coherent-plane reference beam.

The field at the plate due to the cell beam may be written

$$V_T(z) = f(z) \exp \{ i [ \phi_T(z) + \alpha(z) ] \}, \quad (61)$$

where  $T$  is the sample temperature during the recording process. The function  $\alpha(z)$  accounts for constant phase distortions introduced by the cell windows and other intervening optics. After development, the resulting hologram is replaced and illuminated by the cell beam alone, keeping the sample temperature fixed. The original plane-reference wave is then reconstructed, and one observes a diffraction-limited spot in the  $F$  plane behind lens  $L_2$ . If the sample temperature is now changed to  $T' \neq T$ , then the field in the reference direction will no longer be a plane wave, but will be modulated by a factor  $\exp[i(\phi_{T'} - \phi_T)]$ . In this reconstruction, the constant phase distortions are canceled. In practice, the hologram is recorded with the fluid at high temperature ( $T - T_c \sim 60^\circ\text{C}$ ), so that the density distribution is essentially homogeneous and  $\phi_T \approx \phi_\infty = \text{constant}$ . The resulting reconstruction then synthesizes a "cell" with perfect windows. Employing this technique, refraction angles are measured down to the diffraction limit defined by the cell aperture. (See supercritical compressibility, Fig. 10).

#### E. Angle calibration and measurement

The zero reference for angle measurement is determined with the cell in place, at a high temperature where the density gradient is negligible. A plane-wave reference is inserted collinear with the cell beam after transmission, and adjusted to form a diffraction spot at zero angle, thus recording a fixed point on the film records. Angle calibration is accomplished by replacing the cell with a Ronchi ruling of known line spacing, typically 150 lines/in.

The refraction angles  $k_s$  of the interference minima are measured using a precision film-scanning machine (Vanguard Model No. G/J 7039) normally employed in the collection of data from bubble-chamber experiments. For each isotherm, the temperature, minima order numbers, and refraction angles are digitized and recorded on paper tape for subsequent computer analysis. Variances in the angle measurements are estimated by measuring the minima of a single isotherm several times and checking measurement consistency.

Thermal equilibrium was accessed by measuring the angle (compressibility) of several minima as a function of time. The fluid was said to be equilibrated when the angle change over several hours was within the measurement noise. (Competing processes are involved in equilibration,

namely, diffusion and convection. Relaxation times observed were, in general, about three to five times shorter than a worst-case thermal diffusivity calculation would yield. Most likely this is due to the presence of some convection during a temperature change, which is not surprising due to the strong divergence of the Rayleigh number near the critical point.)

## VI. DISCUSSION

### A. The coexistence curve

In this experiment we have measured the xenon coexistence curve in the temperature range  $10^{-5} < |\epsilon| < 10^{-1}$ . The data are represented by the asymptotic power law  $(\rho_L - \rho_G)/\rho_c = 3.51(-\epsilon)^{0.344}$ , but significant systematic deviations remain. Varying the range of fit, we find  $\beta = 0.377$  for  $|\epsilon| < 10^{-3}$  and  $\beta = 0.353$  for  $|\epsilon| > 10^{-3}$ . Similar departures from the asymptotic form  $\Delta\rho^* = B(-\epsilon)^\beta$  have been reported. Stacy *et al.*<sup>26</sup> have observed a temperature-dependent "effective exponent" for xenon which decreases from  $\beta^* = 0.365$  at  $|\epsilon| = 3 \times 10^{-3}$  to  $\beta^* = 0.345$  at  $|\epsilon| = 3 \times 10^{-4}$ . Their sample, however, contained 1% oxygen, and little is known of the effects of impurities on critical behavior. Cornfeld and Carr<sup>27</sup> have determined that  $\beta = 0.37$  in the range  $3 \times 10^{-3} < |\epsilon| < 3 \times 10^{-1}$ , for xenon. Using a technique identical to ours, Balzarini and Ohrn<sup>28</sup> have measured the coexistence curve of sulfur hexafluoride (SF<sub>6</sub>), and found  $\beta = 0.339$  for  $|\epsilon| < 5 \times 10^{-3}$  and  $\beta = 0.346$  for  $|\epsilon| > 10^{-2}$ . Examination of coexistence-curve data in the review of Heller<sup>29</sup> reveals a general tendency for  $\beta$  to increase with increasing  $|\epsilon|$ . Quantitative comparison with this older data is difficult, however, and one rarely encounters a deviation plot.

We are tempted to believe that the observed behavior of the exponent  $\beta$  is due to higher-order corrections to the power law  $\Delta\rho^* = B(-\epsilon)^\beta$ . Addition of a term  $A(-\epsilon)^{\beta'}$  yields  $\beta = 0.332$ ,  $\beta' = 0.61$ , with  $A = 0.93$ . The exponent  $\beta'$  is surprisingly close to  $2\beta$ ; whether this may be expected on theoretical grounds is not clear. Models which display phase transitions generally yield only asymptotic behavior of anomalous properties, with higher-order terms being difficult, if not impossible, to obtain. There is now strong theoretical evidence<sup>30-33</sup> that the rectilinear diameter of a simple fluid is singular, being described as  $\rho_L + \rho_G = 2\rho_c[1 + a|\epsilon|^{1-\alpha}]$ . Experimental verification of such a behavior is difficult, and results to date have been mixed.<sup>34-36</sup> Such a singularity in the diameter could lead to a correction term proportional to  $|\epsilon|^{1-\alpha}$  in the expression describing the coexistence curve. Our observation that  $\beta' = 0.61$  is not consistent with such a correction, since typically  $\alpha \approx 0.1$ . Explan-

ation of the observed behavior must await further theoretical and experimental guides.

### B. The isothermal compressibility

We have measured the isothermal compressibility  $(\partial\mu^*/\partial\rho^*) = P_c K_T$  of xenon along the critical isochore in the temperature range  $10^{-5} < \epsilon < 10^{-1}$ . Assuming an asymptotic power law  $P_c K_T = \Gamma\epsilon^{-\gamma}$ , the results imply  $\gamma = 1.260$ ,  $\Gamma = 0.056$ . For  $\epsilon < 10^{-3}$ , the resultant exponent is  $\gamma = 1.232 \pm 0.006$  with  $\Gamma = 0.073$ . This latter result agrees well with the value of  $\gamma$  obtained in light-scattering experiments.<sup>16,37</sup> We observe a slight tendency for  $\gamma$  to increase for large  $\epsilon$ . This tendency may be noted in the older work of Habgood and Schneider<sup>38</sup> who found  $\gamma = 1.4$  for  $\epsilon > 10^{-3}$  and  $\gamma = 1.0$  for  $\epsilon < 10^{-3}$ . Again, theoretical guidance as to corrections to asymptotic behavior is lacking.

### C. The equation of state

Based upon Widom's assumption concerning the homogeneity of thermodynamic functions and the subsequent work of Schofield and Josephson, we have formulated a new parametric representation for the equation of state of a simple fluid (or a ferromagnet) near the critical point. The new phenomenological transformation is ideally suited to the analysis of data from optical interferometric experiments. We feel the optical technique to be the simplest and most precise means of studying a condensing fluid in the immediate neighborhood of the phase transition ( $-10^{-4} < \epsilon < 10^{-4}$ ), and it is also an ideal complement to conventional PVT measurements, which become difficult and then impossible as the critical point is approached. Previous concerns about the accuracy of information obtained in interferometric experiments have, we believe, been laid to rest by calculations which show that corrections to the Airy-function (cubic) approximation are small.<sup>21</sup>

The new parametric representation suggests a new interpretation of what is meant by the critical temperature. Within the scaling hypothesis, experimentally determined quantities  $\psi_*$  and  $\kappa_T$  are related to the function  $W(\theta)$  by  $d \ln \psi_*/d \ln(1/\kappa_T) = (\beta/\gamma)W(\theta)$ , with  $\theta = \epsilon\kappa_T^{1/\gamma}$ . When this relation is applied to experimental isotherms of xenon, we determine quite readily  $T_c = T_c(\text{lab}) \pm 0.0001$  K. This new technique avoids the divergences and extrapolation errors which occur using conventional definitions. This method appears capable of a very precise absolute determination of  $T_c$  in a fluid. The thermometer used in this work was not calibrated to an international scale, but is within 0.1 K of absolute accuracy.

The scaling hypothesis appears to be well verified for xenon. The direct test employed in Sec.

IV C 2 indicates that scaled variables lie on a single curve. We have placed particular emphasis upon the bilinear function

$$W(\theta) = \frac{1 - \theta/\theta_x}{1 - \theta/\theta_0}. \quad (10)$$

This is the simplest form which satisfies the physical requirements  $W(\theta_x) = 0$ ,  $W(0) = 1$ ,  $W(\theta_0) \rightarrow \infty$ . Integration of  $W(\theta)$  yields the equation of state:

$$Y^{\beta}(R, \epsilon) = Y_0^{\beta} R^{\beta} (1 - \theta/\theta_0)^{\beta\Delta},$$

which introduces the new parameter  $\Delta = 1 - \theta_0/\theta_x$ . The resultant value  $\beta\Delta = 1.38$  is in disagreement with the parametric transformation of Ho and co-workers,<sup>10,39</sup> which implies  $\beta\Delta = 1.50$ . We see a positive advantage in allowing  $\Delta$  to be a free parameter unless and until its value can be deduced from fundamental theory.

The equation of state resulting from the bilinear form Eq. (10) well represents the experimental data for xenon, as indicated by the deviation plot, Fig. 15. Future work will include investigations into the effect of higher-order terms in an expansion of  $W(\theta)$ .

Of the exponents determined by equation-of-state data, the value  $\beta = 0.352$  is somewhat larger than direct coexistence-curve measurements allow. The reason for this behavior is not known. Also of interest is the value of the exponent  $\eta$ , which was introduced by Fisher to account for departure of the pair-correlation function from the Ornstein-Zernike result. From the scaling law  $\eta = 2 - 3(\delta - 1)/(\delta + 1)$ , the present work indicates (see Table II) that  $\eta \approx 0.101$ , which is within the  $\eta$  range from the refractive-index measurements of Hocken.<sup>17</sup> From turbidity measurements on the binary mixture cyclohexane, Calmettes and co-workers<sup>40</sup> find  $\eta = 0.08 \pm 0.5$ . The large uncertainty reflects the difficulty involved in direct measurements of  $\eta$ .

The compressibility exponent  $\gamma$  is found to be 1.230 from equation-of-state data. This is consistent with the direct supercritical compressibility measurements, which indicate  $\gamma = 1.232$  for  $\epsilon < 10^{-3}$ .

Throughout this paper we have used the statistical estimates for our parameter uncertainties. The choice of the model clearly alters these best-fit parameters by more than the statistics would allow (see Table I). This model dependency is not unexpected; in fact, we display the statistical uncertainties only to make this point more graphic. Since we have no *a priori* knowledge of the truth of any model, we might rely entirely on our statistics. If we do this the model of Table I(a) is the favorite due to the low  $\chi^2$  and large data set. On the other hand, the  $\beta$  obtained from fits of Fraunhofer data to this equation is in clear contra-

dition to the limiting  $\beta$  obtained from the more direct coexistence-curve measurements. Even if we do not trust the statistics and assume all models are equivalent, we must stretch our errors more than we would readily believe in order to make all three experiments (coexistence curve, compressibility, and equation-of-state) yield overlapping parameters within the same region. We consciously chose not to do this because we believe that this difference is outside our errors and thus yields information about either the choice of model or residual systematic errors in the experiments. We are still working on this problem.

#### ACKNOWLEDGMENTS

The authors appreciate numerous helpful discussions with Professor George Stell. Thanks are also due to Dr. J. M. H. Levelt Sengers and to Dr. David Balzarini. We also appreciate the assistance of the bubble-chamber group at the State University of New York at Stony Brook for making the film-scanning apparatus available to us.

#### APPENDIX: EQUIVALENCE OF THE $W$ HYPOTHESIS AND THE HO-LITSTER REPRESENTATION FOR $\beta\Delta = 3/2$

Ho and Litster<sup>10</sup> have introduced the following parametric representation:

$$\mu = a\phi(1 - \phi^2)r^{\beta\delta}, \quad (A1a)$$

$$\rho = k\phi(1 - c\phi^2)r^{\beta}, \quad (A1b)$$

$$\epsilon = (1 - b^2\phi^2)r, \quad (A1c)$$

$$c = (3 - 2\beta\delta)/(3 - 2\beta). \quad (A1d)$$

When the parameter  $b^2$  takes on the value

$$b^2 = 3/(3 - 2\beta), \quad (A1e)$$

lines of constant  $r$  correspond to paths of constant compressibility (susceptibility), so that  $(\partial\mu/\partial\rho)_{\epsilon}$  is independent of  $\phi$ . The critical isochore is  $\phi = 0$ , the critical isotherm  $\phi = \pm b^{-1}$ , and the coexistence boundary  $\phi = \pm 1$ . The transformation involves five parameters:  $\beta$ ,  $\gamma$ ,  $T_c$ ,  $a$ , and  $k$ . In this Appendix we demonstrate the equivalence of Eqs. (A1) and the parametric equations resulting from the  $W$  hypothesis, constraining the parameter combination  $\beta\Delta$  to the value  $\frac{3}{2}$ .

Equating Eqs. (A1c) and (3) for equal values of  $\epsilon$ , we have

$$\epsilon = (1 - b^2\phi^2)r = R\theta. \quad (A2)$$

On the critical isochore,  $\phi = 0$  and  $\theta = \theta_0$ , whence

$$r = R\theta_0, \quad (A3)$$

thus

$$1 - b^2\phi^2 = \theta/\theta_0. \quad (A4)$$

At the coexistence boundary,  $\phi = \pm 1$  and  $\theta = \theta_x$ , so that Eqs. (A2) and (A3) imply

$$1 - b^2 = \theta_x / \theta_0. \quad (\text{A5})$$

Then, using Eq. (A4), we have

$$\phi^2 = \frac{1 - \theta / \theta_0}{1 - \theta_x / \theta_0}. \quad (\text{A6})$$

The ratio  $\theta_x / \theta_0$  in the Ho-Litster model becomes, from Eq. (A5) and the definition Eq. (A1e),

$$\theta_x / \theta_0 = 1 - b^2 = -2\beta / (3 - 2\beta), \quad (\text{A7})$$

so that with the definition  $\Delta = 1 - \theta_0 / \theta_x$  of the *W* hypothesis [Eq. (12)], we obtain

$$1 / (1 - \Delta) = -2\beta / (3 - 2\beta), \quad (\text{A8})$$

which requires

$$\beta\Delta = \frac{3}{2}. \quad (\text{A9})$$

Thus, the *W* hypothesis identically reproduces the Ho-Litster representation when  $\beta\Delta$  is constrained to satisfy relation (A9). The parameters in the two models are related according to the following translation:

<i>W</i> hypothesis	Ho-Litster
$R\theta_0$	$r$
$\frac{1 - \theta / \theta_0}{1 - \theta_x / \theta_0}$	$\phi^2$
$1 - \theta_x / \theta_0$	$b^2$
$\theta_0^{-\gamma}$	$a/k$

\*Based upon Ph.D. thesis of W. T. Estler; work supported in part by the National Science Foundation.

†Present address: Physics Department, New College, Sarasota, Florida 33578.

‡Present address: Heat Division, National Bureau of Standards, Washington, D. C. 20234.

<sup>1</sup>Kadanoff *et al.*, Rev. Mod. Phys. **39**, 395 (1967).

<sup>2</sup>B. Widom, J. Chem. Phys. **43**, 3898 (1965).

<sup>3</sup>L. P. Kadanoff, Physics **2**, 263 (1966).

<sup>4</sup>R. B. Griffiths, Phys. Rev. **158**, 176 (1967).

<sup>5</sup>L. R. Wilcox and W. T. Estler, J. Phys. (Paris) **32**, C52-175 (1971).

<sup>6</sup>P. Schofield, Phys. Rev. Lett. **22**, 606 (1969).

<sup>7</sup>B. D. Josephson, J. Phys. C **2**, 1113 (1969).

<sup>8</sup>L. R. Wilcox and D. Balzarini, J. Chem. Phys. **48**, 753 (1968).

<sup>9</sup>D. Balzarini, Ph.D. thesis (Columbia University, 1968) (unpublished).

<sup>10</sup>J. T. Ho and J. D. Litster, Phys. Rev. B **2**, 4523 (1970).

<sup>11</sup>C. L. Gouy, C. R. Acad. Sci. (Paris) **90**, 307 (1880).

<sup>12</sup>G. Kegeles and L. J. Gosting, J. Am. Chem. Soc. **69**, 2516 (1947).

<sup>13</sup>L. J. Gosting, E. M. Hanson, G. Kegeles, and M. S. Morris, Rev. Sci. Instrum. **20**, 209 (1949).

<sup>14</sup>L. J. Gosting and L. Onsager, J. Am. Chem. Soc. **74**, 6066 (1952).

<sup>15</sup>D. H. Garside, H. V. Molgaard, and B. L. Smith, J. Phys. B **1**, 449 (1968).

<sup>16</sup>M. Giglio and G. B. Benedek, Phys. Rev. Lett. **23**, 1145 (1969).

<sup>17</sup>R. Hocken, Ph.D. thesis (S.U.N.Y. at Stony Brook, 1973) (unpublished).

<sup>18</sup>M. Vicentini-Missoni, J. M. H. Levelt Sengers, and M. S. Green, J. Res. Natl. Bur. Stand. (U. S.) A **73**, 563 (1969).

<sup>19</sup>G. N. Watson, *Theory of Bessel Functions*, 2nd ed. (Cambridge U. P., Cambridge, 1944).

<sup>20</sup>M. Abramowitz and I. A. Stegun, *Handbook of Mathematical Functions* (Dover, New York, 1965).

<sup>21</sup>W. T. Estler, Ph.D. thesis (S.U.N.Y. at Stony Brook, 1972) (unpublished).

<sup>22</sup>J. S. Kouvel and M. E. Fisher, Phys. Rev. **136**, 1626 (1964).

<sup>23</sup>P. R. Bevington, *Data Reduction and Error Analysis for the Physical Sciences* (McGraw-Hill, New York, 1969).

<sup>24</sup>P. Schofield, J. D. Litster, and J. T. Ho, Phys. Rev. Lett. **23**, 1098 (1969).

<sup>25</sup>A. W. Warner, Bell Systems Tech. J. **39**, 5 (1960).

<sup>26</sup>L. M. Stacy, B. Pass, and H. Y. Carr, Phys. Rev. Lett. **23**, 1424 (1969).

<sup>27</sup>A. B. Cornfeld and H. Y. Carr, Bull. Am. Phys. Soc. **17**, 277 (1972).

<sup>28</sup>D. Balzarini and K. Ohrn, Phys. Rev. Lett. **29**, 840 (1972).

<sup>29</sup>P. Heller, Rep. Prog. Phys. **30**, 731 (1967).

<sup>30</sup>B. Widom and J. S. Rowlinson, J. Chem. Phys. **52**, 1670 (1970).

<sup>31</sup>N. D. Mermin, Phys. Rev. Lett. **26**, 169 (1971).

<sup>32</sup>N. D. Mermin, Phys. Rev. Lett. **26**, 957 (1971).

<sup>33</sup>P. C. Hemmer and G. Stell, Phys. Rev. Lett. **24**, 1284 (1970); J. Chem. Phys. **56**, 4274 (1972).

<sup>34</sup>J. M. H. Levelt Sengers, J. Straub, and M. Vicentini-Missoni, J. Chem. Phys. **54**, 5034 (1971).

<sup>35</sup>J. Weiner, K. H. Langley, and N. C. Ford, Jr., Phys. Rev. Lett. **32**, 16 (1974); 879 (1974).

<sup>36</sup>A. B. Cornfeld and H. Y. Carr, Phys. Rev. Lett. **29**, 28 (1972).

<sup>37</sup>I. W. Smith, M. Giglio, and G. B. Benedek, Phys. Rev. Lett. **27**, 1556 (1971).

<sup>38</sup>H. W. Habgood and W. G. Schneider, Can. J. Chem. **32**, 98 (1954).

<sup>39</sup>C. Huang and J. T. Ho, Phys. Rev. A **7**, 1034 (1973).

<sup>40</sup>P. Calmettes, I. Lagues, and C. Laj, Phys. Rev. Lett. **28**, 478 (1972).

FIG. 4.  $F$ -plane intensity distribution  $I(k, T)$  from a sample of xenon. This sweep took about 24 h. Divergence of fringes for  $T \rightarrow T_c^+$  reflects the diverging isothermal compressibility; disappearance of fringes for  $T < T_c$  indicates a density discontinuity, i.e., the coexistence boundary. Any fringe, maximum, or minimum, is a locus of constant optical phase.

